

Published in IET Power Electronics
 Received on 19th April 2013
 Revised on 20th September 2013
 Accepted on 17th October 2013
 doi: 10.1049/iet-pel.2013.0292



ISSN 1755-4535

Reduced order generalised integrator-based current controller applied to shunt active power filters

Sebastian Gomez Jorge, Claudio A. Busada, Jorge Solsona

Departamento de Ingenieria Electrica y de Computadoras, Instituto de Investigaciones en Ingenieria Electrica, Universidad Nacional del Sur – CONICET, Avda. Alem 1253, Bahía Blanca 8000, Argentina
 E-mail: sebastian.gomezjorge@uns.edu.ar

Abstract: This study proposes the application of a current controller based on the reduced order generalised integrator (ROGI) to control a three-phase three-wire shunt active power filter (SAPF). The ROGI-based controller has low computational burden and it is suitable for its implementation in low-cost digital signal processors (DSPs). This controller is also frequency adaptive. This allows it to maintain its high steady-state performance despite grid frequency variations. Unlike conventional high performance SAPFs this current controller does not require the computation of high quality current references (with low distortion and total harmonic distortion below that recommended by the IEEE Std 519-1992). Therefore most of the available computational power can be used for compensating the harmonics produced by the load.

1 Introduction

Nowadays the usage of non-linear loads is common, in both domestic and industrial levels. A non-linear load connected to the grid produces currents with harmonic content, and this content degrades the quality of the grid voltage at the point of common coupling (PCC). The IEEE Std 519-1992 [1] describes recommendable practices regarding the production of harmonic currents by the consumer. The most restrictive recommendations are given for the large consumers, whose consumption must have a total harmonic distortion (THD) of less than 5%.

Complying with this recommendation has been the goal of many researchers. Among the means developed to do so, the active filters can be highlighted. In recent years, one of the main focuses of research of the active filters has been the shunt active power filter (SAPF) [2–6]. In what follows, some relevant results obtained to this date on this field are briefly described. In [2], a discrete time repetitive controller implemented in a rotating dq frame is designed considering that the system is fed by a pure sinusoidal grid voltage. The proposal is capable of reactive power compensation and of load unbalance compensation. However, in order to work properly, the algorithm requires the sampling frequency to be a multiple of the grid frequency. Therefore its performance degrades in presence of frequency variations. In [3], a recursive method to obtain a current reference with low distortion, synchronised with the grid is proposed. This method is based on the structure ‘Park transform-low pass filter-Park antitransform’. The authors prove that the method is sensitive to frequency variations, and present a frequency adaptive variant which uses a phase locked loop (PLL). The proposal is used to generate the current reference for a current controller based on

second-order generalised integrators (SOGIs), [7]. The implementation of this controller requires the measurement of the load and SAPF currents. In [4], the load current is controlled using a SAPF with a proportional-integral (PI) controller implemented in the rotating dq frame. The controller gains are computed through the theory of the linear quadratic regulator (LQR). In this case, the synchronisation is also achieved through a PLL, and the implementation requires the measurement of the load and SAPF currents. A different approach is proposed in [5], the plant model parameters are estimated through variable structure, and these parameters are used to tune the gains of a controller, online, through pole placement. The scheme is implemented in the rotating dq frame, synchronised through a PLL. The controller shows good performance, even in presence of unbalanced grid voltages. In [6], a current controller for the SAPF which is based on SOGIs is proposed. In this paper, the SAPF is implemented using an LCL coupling filter with active damping. A methodology to choose the parameters of the coupling filter and the active damping system is also proposed. The proposed control scheme is also implemented in the rotating dq frame and synchronised through a PLL. In [8], an improved predictive current controller for SAPF is proposed. The proposal is based on the conventional dead-beat controller, and improves upon it by compensating the delays of its digital implementation. This is done by predicting the state of the system one and two sampling instants ahead. The proposal is more robust to noise than the conventional dead-beat controller, and it is also robust to parametric uncertainties, although its performance is affected by these. Suresh *et al.* [9] proposed an adaptive fuzzy hysteresis current controller for SAPFs. The application of the fuzzy logic control (FLC) increases the robustness to parameter uncertainties and

achieves an improved steady state and transient tracking performance when compared to the traditional PI controller. In [10], the application of FLC with different member functions to an instantaneous real active and reactive component control strategy is studied. The controller is used to improve the performance of a SAPF under balanced, unbalanced and distorted grid voltage conditions. It is concluded that using Gaussian member functions outperforms other member functions and PI controllers, complying with the IEEE Std 519-1992 recommendations on harmonic levels.

Most of the strategies described above are implemented in a rotating dq frame and assume that the grid voltage is a pure sinusoid, which allows them to achieve the synchronisation through simple algorithms [e.g. the synchronous reference frame PLL (SRF-PLL) [11]]. However, in some cases the grid voltage at the PCC can be distorted. In these cases, the synchronisation algorithm must be immune to the highest harmonic component that the SAPF is expected to reject. Otherwise, the current references generated by the synchronisation algorithm will contain these harmonics. The required immunity can be achieved through a SRF-PLL with slow transient response. This attained at the expense of reducing the SAPF convergence speed to frequency or voltage variations, which may not be acceptable in some applications. Synchronisation strategies with fast convergence speed and low distortion are usually more complex than a SRF-PLL [12–14], and their implementation increases the required computational power significantly. This reduces the resources available for the current controller, which can be critical in a low-cost digital signal processor (DSP) application.

This paper proposes the use of a ROGI-based current controller to control a three-phase SAPF. The controller is implemented in the stationary reference frame and it is based on ROGIs [15]. The features of this controller are as follows: it compensates high-order harmonics, reducing the distortion of the grid-side currents, in compliance with the IEEE Std 519-1992, even when the grid voltage is highly distorted; it does not require accurate current references, nor current references that must be updated quickly in presence of load transients or grid voltage transients. This saves the computational load required to generate these.

To maintain its performance in presence of grid frequency variations, a frequency adaptation algorithm is required [16]. To this end, a new frequency estimation algorithm is proposed here. This algorithm reduces the estimated frequency ripple, it is simple, has fast convergence speed and low-computational burden. The main contribution of this paper is therefore

2-fold: it shows that the ROGI-based current controller can be used in SAPF applications; and it proposes a new frequency estimation algorithm to use with this current controller. The low-computational burden of the whole control and frequency estimation algorithm makes it ideal for its implementation in low-cost DSPs.

The paper is organised as follows. In Section 2, a description of the system under study is presented. Section 3 describes the current controller and the proposed frequency estimator. Also, in this section, an analysis of coupling inductor uncertainties is performed. In Section 4, the simulation and experimental results are shown. Finally, conclusions are drawn in Section 5.

2 System description

Fig. 1 shows the topology of the system under study. It is composed of a non-linear load and a SAPF, both connected to a three-phase three-wire grid. The SAPF is composed of a coupling inductor L_f , a high frequency filtering capacitor C_f , a voltage source converter (VSC), a dc bus capacitor C and a controller. The grid impedance, seen from the PCC, is modelled by the inductor L_g . Also, depending on the nature of the non-linear load the system might have a smoothing inductor L_l , connected between the non-linear load and the PCC. This inductor is used to smooth the steep flanks of the load current that cannot be compensated by the SAPF.

For simplicity, in this figure, the three-phase signals are denoted with the superscript RST . To perform the control, the measurement of three-phase voltages at the PCC (V_g^R , V_g^S and V_g^T), two-grid phase currents (I_g^R and I_g^S) and the dc bus voltage (V_{dc}) are required.

The measured ac signals are transformed to the stationary reference frame through Clarke's transform, and are expressed throughout this paper using complex notation [17]. The transformation of the signals V_g^R , V_g^S and V_g^T results in the complex signal $v_g = v_{g\alpha} + jv_{g\beta}$, and the transformation of the signals I_g^R and I_g^S results in the complex signal $i_g = i_{g\alpha} + ji_{g\beta}$, where $j = \sqrt{-1}$. From now on, all the ac signals will be considered on the stationary reference frame unless otherwise stated.

3 ROGI-based controller

Fig. 2 shows the plant model and the ROGI-based controller. The signals i_g , i_f , i_{nl} , v_g and v_f are defined applying Clarke's transform to their RST versions defined in Fig. 1.

The block PLANT represents the continuous time model of the plant, which is the coupling inductance L_f connected between v_g and v_f , whose current is added to the load current i_{nl} to obtain the grid current i_g . The block CONTROLLER represents the proposed controller, and it is subdivided in three additional subblocks: bus controller, current controller and frequency estimator, which are described in what follows.

3.1 Bus controller

This controller is responsible for regulating the mean value of the bus dc voltage V_{dc} to its reference value V_{dc}^* . It consists of a PI regulator, whose input and output are the error signal $V_{dc} - V_{dc}^*$ and the signal g , respectively. The output signal g is used to synthesise the current reference i_g^* of the current

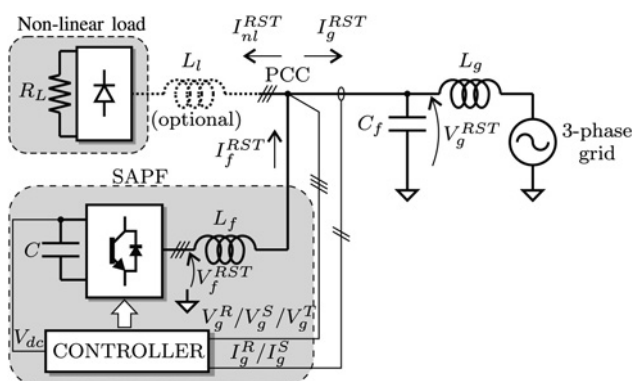


Fig. 1 System description

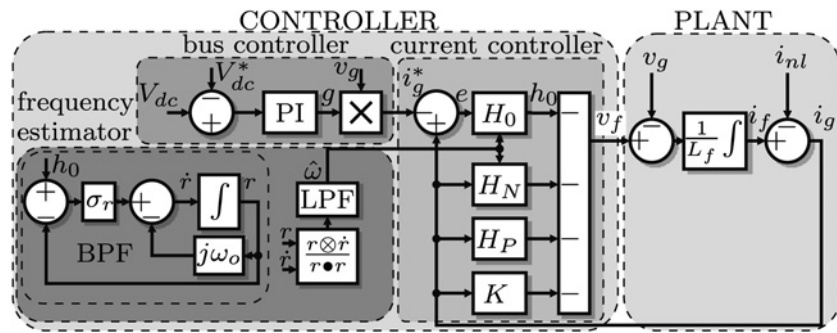


Fig. 2 Plant model and ROGI-based controller

controller block. This reference is

$$i_g^* = g v_g \quad (1)$$

As will be shown in the following, the signal g defines the amplitude of the fundamental component of the current drained from the grid by the SAPF-load set.

3.2 Current controller

3.2.1 General description: This controller must fulfill three objectives:

- (a) It must ensure that in steady state the grid current i_g follows the positive sequence fundamental component of the grid voltage v_g .
- (b) It must be immune to the harmonics present at the PCC voltage. This means that in absence of load, the controller must be able to regulate its current at the necessary value to stay operative, without introducing harmonics on its own.
- (c) It must ensure that, in steady state, i_g does not contain harmonics of the fundamental frequency.

The objective (a) is achieved through the differential equation

$$\dot{h}_0 = K_0 e + j\hat{\omega} h_0 \quad (2)$$

where e is the input, K_0 is a design constant and $\hat{\omega}$ is the estimated frequency of the positive sequence fundamental component of the PCC voltage (whose frequency is ω). This differential equation can be represented in a compact form through the input–output relation (IOR) H_0 shown in Fig. 2, that is defined as

$$H_0 = \frac{h_0}{e} = \frac{K_0}{p - j\hat{\omega}} \quad (3)$$

where p is the derivative operator. The IORs H_N and H_P shown in Fig. 2, which will be described shortly, will be ignored for the time being. The IOR (3) implements a ROGI tuned at frequency $\hat{\omega}$, hence it has infinite gain to an input signal of positive sequence and frequency $\hat{\omega}$. Also, it has low gain to all other frequencies, and for negative sequence signals [15]. This implies that, if the closed loop system is stable, the error signal $e = i_g - i_g^*$ defined in Fig. 2 that enters H_0 cannot contain positive sequence harmonics of frequency $\hat{\omega}$, once the steady state is reached. Naturally, this implies that i_g will follow the positive sequence component of frequency $\hat{\omega}$ present in i_g^* . If $\hat{\omega}$ is

equal to the fundamental frequency ω of the grid voltage and $g = \text{const.}$, (which happens in steady state), from (1) it is concluded that i_g will copy the positive sequence fundamental component of the grid voltage v_g and that its amplitude will be g times that of this component. This verifies that H_0 fulfills objective (a). Also, it is verified that g in (1) defines the amplitude of i_g .

The objectives (b) and (c) are achieved through the IORs H_N and H_P of Fig. 2, which are defined as

$$H_N = \sum_{n=1}^N \frac{K_{-(6n-1)}}{p + j(6n-1)\hat{\omega}} \quad (4)$$

$$H_P = \sum_{n=1}^P \frac{K_{(6n+1)}}{p - j(6n+1)\hat{\omega}} \quad (5)$$

where N is the total number of negative sequence harmonics to compensate, P is the total number of positive sequence harmonics to compensate and $K_{-(6n-1)}$ and $K_{(6n+1)}$ are design constants. Equation (4) is a summation of ROGIs tuned to the multiples $-5, -11, -17, \dots, -(6N-1)$ of $\hat{\omega}$ and (5) a summation of ROGIs tuned to the multiples $7, 13, 19, \dots, (6P+1)$ of $\hat{\omega}$. This means that H_N has infinite gain to negative sequence signals of frequencies $5, 11, 17, \dots, (6N-1)$ times $\hat{\omega}$ and H_P to positive sequence signals of frequencies $7, 13, 19, \dots, (6P+1)$ times $\hat{\omega}$. Therefore, if the gains are properly chosen so that the system is closed-loop stable, i_g will not contain either harmonics of those frequencies or sequences once steady state is reached. Then, if $\hat{\omega} = \omega$, $g = \text{const.}$ and H_N and H_P model all the harmonics of i_{nl} , the current i_g will not contain them once the steady state is reached. Also, the harmonic content of i_{nl} is that of the grid voltage plus the harmonics produced by the non-linear load. Therefore, modelling all the harmonics of i_{nl} in H_N and H_P guarantees immunity to the harmonics present in the PCC voltage. The choice of those harmonic successions previously described is not arbitrary, since these are the dominant harmonic sequences in three-phase systems with normal imbalances ($<3\%$ unbalance [18]).

3.2.2 Choice of gains: As detailed in [15], the ROGI-based controller implements a full state feedback. As the current i_g is a system state, the constant K defined in Fig. 2 is the gain of this state. The value of K and of the gains of (3) and (4) can be obtained through the LQR theory [19], which requires to know the system's open-loop model described in state variable form. For the system of Fig. 2, opening the feedback path from i_g to the block

current controller, the open-loop model results

$$\dot{\mathbf{x}} = \mathbf{A}\mathbf{x} + \mathbf{B}v_f \quad (6)$$

where

$$\mathbf{A} = \begin{bmatrix} 0 & 0 & 0 & 0 & \dots & 0 & 0 \\ 1 & j\hat{\omega} & 0 & 0 & \dots & 0 & 0 \\ 1 & 0 & -5j\hat{\omega} & 0 & \dots & 0 & 0 \\ 1 & 0 & 0 & j7\hat{\omega} & \dots & 0 & 0 \\ \vdots & \vdots & \vdots & \vdots & \ddots & \vdots & \vdots \\ 1 & 0 & 0 & 0 & \dots & -(6N-1) & 0 \\ 1 & 0 & 0 & 0 & \dots & 0 & (6P+1) \end{bmatrix} \quad (7)$$

$$\mathbf{B} = [1/L_f \ 0 \ 0 \ 0 \ \dots \ 0 \ 0]^T \quad (8)$$

The state vector is defined as $\mathbf{x} = [i_f \ r_0 \ r_{-5} \ r_7 \ \dots \ r_{-(6N-1)} \ r_{(6P+1)}]^T$ where r_n is the output of the n th IOR defined in (4) or in (5), before the multiplication by its corresponding gain. The choice of the parameters \mathbf{Q} and \mathbf{R} of the LQR theory is made as described in [20].

3.2.3 Steady-state response: To verify that the ROGI-based controller fulfills the objectives (a)–(c) of Section 3.2, the effect of the signals i_g^* , v_g and i_{nl} on the grid current i_g will now be analysed. In order to do so, the closed-loop frequency response of i_g to those signals will be found, assuming that the system has reached steady state ($g = \text{const.}$ and $\hat{\omega} = \omega$). The state variable description of the closed-loop system results

$$\dot{\mathbf{x}} = \mathbf{A}_{cl}\mathbf{x} + \mathbf{B}_v v_g + \mathbf{B}_i i_g^* + \mathbf{B}_{nl} i_{nl} \quad (9)$$

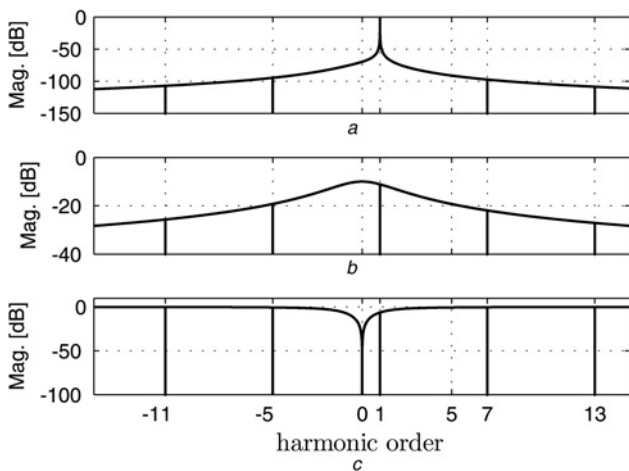


Fig. 3 Bode diagrams with the frequency axis normalised with respect to $\hat{\omega}$

- a $|I_g/I_g^*|(j\Omega)$
- b $|I_g/V_g|(j\Omega)$
- c $|I_g/I_{nl}|(j\Omega)$

Table 1 Parameters

Parameters	Five value	Five description
v_g	110 Vrms	grid voltage
ω_0	$2\pi 50$ rad/s	nominal freq.
L_g	90 μ H	grid impedance
L_f	5.5 mH	coupling ind.
C_f	1 μ F	high freq. cap.
C	330 μ F	dc bus cap.
L_l	0 [unless otherwise stated]	smooth ind.
R_L	70 Ω	load resistor
Controller		
T_s	100 μ s	sample time
V_{DC}^*	500 V	dc bus ref.
K_{pPI}	0.001 A/V	bus PI prop. gain
K_{iPI}	0.01 A/V	bus PI inte. gain
N	28 [ROGIs]	ROGI quantity
R	10	LQR scalar
\mathbf{Q}	diag([100 100 1 ... 1])	LQR matrix
σ_r	200 rad/s	BPF cut-off
σ	100 rad/s	LPF cut-off

where $\mathbf{A}_{cl} = \mathbf{A} - \mathbf{B}\mathbf{K}$

$$\mathbf{K} = [K \ K_0 \ K_{-5} \ K_7 \ \dots \ K_{-(6N-1)} \ K_{(6P+1)}] \quad (10)$$

$$\mathbf{B}_v = -\mathbf{B} \quad (11)$$

$$\mathbf{B}_i = [0 \ -1 \ 0 \ 0 \ \dots \ 0 \ 0]^T \quad (12)$$

$$\mathbf{B}_{nl} = \left[\frac{K}{L_f} \ -1 \ -1 \ -1 \ \dots \ -1 \ -1 \right]^T \quad (13)$$

Then, the frequency responses of interest are obtained through

$$\frac{I_g}{I_g^*}(j\Omega) = \mathbf{C}(j\Omega\mathbf{I} - \mathbf{A}_{cl})^{-1}\mathbf{B}_i \quad (14)$$

$$\frac{I_g}{V_g}(j\Omega) = \mathbf{C}(j\Omega\mathbf{I} - \mathbf{A}_{cl})^{-1}\mathbf{B}_v \quad (15)$$

$$\frac{I_g}{I_{nl}}(j\Omega) = \mathbf{C}j(\Omega\mathbf{I} - \mathbf{A}_{cl})^{-1}\mathbf{B}_{nl} - 1 \quad (16)$$

where $\mathbf{C} = [1 \ 0 \ 0 \ 0 \ \dots \ 0 \ 0]$, I_g , I_g^* , I_{nl} and V_g are the Laplace transforms of i_g , i_g^* , i_{nl} and v_g , respectively, and \mathbf{I} is the identity matrix with the dimensions of \mathbf{A} . In Fig. 3, the magnitudes of these frequency responses are shown, with the frequency axis normalised with respect to the estimated frequency $\hat{\omega}$. These were plotted for a controller with $N=2$ and $P=2$ (that is, cancellation of harmonic sequences -5 , 7 , -11 and 13), whose gains are obtained choosing $\mathbf{Q} = \text{diag}([100 \ 1 \ 1 \ 1 \ 1 \ 1])$ and $R=10$ and applying the LQR theory. The remaining system parameters are shown in Table 1 of Section 4. Fig. 3a shows the magnitude of (14). This response has zeros to the harmonic sequences -11 , -5 , 7 and 13 . This implies that i_g will not contain these harmonic components once steady state is reached, even when they are present in i_g^* . Also, since the frequency response has unitary gain (0 dB) and phase 0° (not shown) to the positive sequence component of frequency $\hat{\omega}$ present in i_g^* , i_g will contain an exact copy of this component once steady state is reached. From (1), it is once again verified that i_g will follow the positive sequence fundamental component of the grid voltage, and that g

determines the amplitude of this current. Fig. 3b shows the magnitude of (15), which describes the effect of v_g harmonics on i_g . In this case, the response has zeros to harmonic sequences $-11, -5, 1, 7$ and 13 . Hence, i_g will not contain these sequences once steady state is reached, even if v_g does. This implies that, if H_N and H_P model all the harmonics of v_g , the controller will be immune to the PCC voltage distortion. This result had already been verified in [15]. However, the computation of the magnitude of (16), which is shown in Fig. 3c, was not previously performed. As can be seen in that figure, this transfer function has the same zeros as (15), plus a dc zero provided by the proportional feedback. Therefore i_g will not have these sequences either, even if i_{nl} does.

The previous analysis guarantees that the harmonics modelled in (4) and (5) are rejected and do not appear in i_g once steady state is reached. Also, the positive sequence component of frequency $\hat{\omega}$ of i_g^* is copied (magnitude and phase) by i_g once steady state is reached. This implies that the controller is capable of producing grid currents with low-distortion level if its ROGIs are tuned to the grid frequency ($\hat{\omega} = \omega$) and if H_N and H_P model all the harmonics of i_{nl} . However, it is clear that if (3)–(5) are not tuned exactly to this frequency, the harmonic cancellation will not be accurate and i_g will be distorted. For this reason, in Section 3.3, a frequency estimator is proposed.

3.2.4 Discretisation: The controller discretisation is performed through pole mapping to the discrete complex plane. This is done through the transformation $e^{-jn\hat{\omega}T_s}$, where $n\hat{\omega}$ is the pole of the n th IOR in the continuous time domain, and T_s is the sample time. This discretisation only adds one additional state to the number of states required for the discrete time implementation of the controller, which corresponds to consider the processing delay as a state of the system. This additional state must be taken into account to improve the controller's stability margins. A detailed analysis of the implementation of this kind of discretised controllers is carried out in [15].

3.2.5 Coupling inductor and grid uncertainties: Once the controller feedback gains are chosen, it is possible to analyse the effect that uncertainties in the value of L_f and L_g have on the closed-loop stability. This can be done plotting the maximum real part of the closed-loop poles of the system as these parameters vary. Fig. 4a shows the

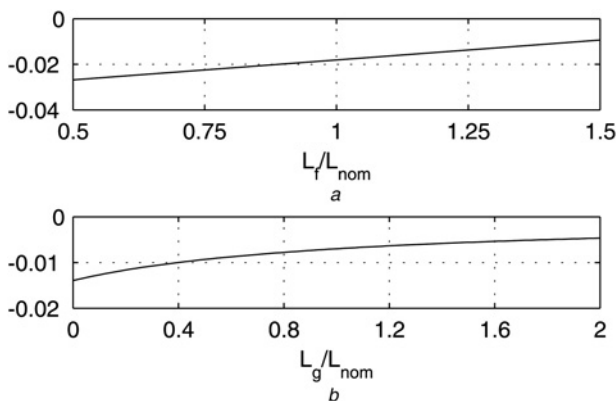


Fig. 4 Effect of uncertainties in the value of L_f and L_g on the closed-loop stability

a Real part of the closed loop poles as L_f varies
b Real part of the closed loop poles as L_g varies

maximum real part of the eigenvalues of A_{cl} for $0.5 < L_f/L_{nom} < 1.5$, where L_{nom} is the nominal value of L_f defined in Table 1 ($L_{nom} = 5.5$ mH). As can be seen, since the real part of all the poles is negative, the system remains stable. Fig. 4a shows the maximum real part of the eigenvalues of $A_{cl} + B_i L_g / (L_f + L_g) K_g$ for $0 < L_g/L_{nom} < 2$. These were plotted for different values of g , however, the effect of g on the pole location is negligible for its typical values ($g \ll 1$). As can be seen, since the real part of all the poles is negative, the system also remains stable. Both figures were plotted for $\hat{\omega} = \omega_0$.

3.3 Frequency estimator

The output of the IOR H_0 is the signal h_0 , as shown in Fig. 2. Since this IOR regulates the fundamental component of i_g , then h_0 will be a sinusoidal signal of angular frequency ω , whose amplitude and phase will be similar to those of the positive sequence fundamental component of v_g (since the voltage drop $v_f - v_g$ on L_f is relatively small). It will also contain the harmonic components present in i_g^* , attenuated by the IOR H_0 . To further attenuate these harmonic components, h_0 is filtered through a band pass filter (BPF), as shown in the block frequency estimator of Fig. 2. This BPF is implemented with a ROGI tuned at the nominal grid frequency $\omega_o = \text{const.}$, and has cut-off frequency σ_r . Its output $r = r_\alpha + jr_\beta$ has instantaneous frequency $\hat{\omega}$, and in steady state the mean value of this frequency will be $\bar{\omega} = \omega$ the value of the fundamental frequency of its input. This frequency can be estimated by definition using r and its derivative, as shown in the following equation

$$\hat{\omega} = \frac{d}{dt} \arctan\left(\frac{r_\beta}{r_\alpha}\right) = \frac{r_\alpha \dot{r}_\beta - \dot{r}_\alpha r_\beta}{r_\alpha^2 + r_\beta^2} = \frac{r \otimes \dot{r}}{r \bullet r} \quad (17)$$

where \otimes is the cross product between the vectors formed by the real and imaginary parts of the signals involved and \bullet is the scalar product of these vectors. Then, ω can be estimated filtering $\hat{\omega}$ with a LPF to obtain its mean value, which results

$$\dot{\omega} = \sigma \left[\text{sat}\left(\frac{r \otimes \dot{r}}{r \bullet r}\right) - \hat{\omega} \right] \quad (18)$$

where σ is the LPF cut-off frequency and $\text{sat}()$ is a function that saturates $\hat{\omega}$ within a set of ω_o . The presence of the saturation is justified, due to the fact that in distribution systems the frequency ω does not show great deviations with respect to ω_0 (in general smaller than 1%). The convergence speed of this estimator will be tightly linked with the non-linear dynamic of the set 'current controller-frequency estimator' plus the BPF dynamic. If these dynamics are fast compared with that of the LPF used in (18), then the convergence speed of (18) is determined by the cut-off frequency of the LPF. According to classic control theory, for a step input, the convergence time of the output of a first-order LPF to 2% of its final value is [19]

$$t_{\text{set}} = \frac{4}{\sigma} \quad (19)$$

which allows to choose σ according to the desired response time.

When compared with the frequency estimator developed in [14], the proposed estimator is conceptually different. In [14],

the frequency is computed through the cross-product of the signals $e = i_g - i_g^*$ (see Fig. 2) and h_0 . The sign of the cross-product indicates whether $\hat{\omega}$ should be increased or decreased, therefore it is integrated to obtain the frequency estimator. However from (1), e has the harmonic content of v_g , therefore $\hat{\omega}$ will have steady-state ripple. In this paper, h_0 is filtered with a BPF and then the instantaneous frequency of the output of this filter is computed by definition. Since the calculation of the frequency by definition has fast transient response, it can lead to instability, because the resulting frequency adaptive current controller is non-linear. Therefore it is filtered with a LPF to decouple the frequency estimator and the current controller dynamics. The resulting frequency estimator has smaller steady-state ripple than that of [14]. This is because of the additional filtering of the BPF.

3.3.1 Discretisation: The discretisation of the BPF is discussed in detail in [14] so only the discretisation of (17) and (18) will be shown. If $r[k]$ is the discrete time version of r at the sampling instant k , it is simple to verify that

$$\frac{r[k-1] \otimes r[k]}{r[k-1] \bullet r[k]} = \tan(\Delta\theta[k]) \quad (20)$$

where $\Delta\theta$ is the phase difference between $r[k]$ and $r[k-1]$, $\Delta\theta = \hat{\omega}[k]T_s$, where $\hat{\omega}[k]$ represents the average value of the frequency $\hat{\omega}$ over time T_s . From this last equation it results that

$$\hat{\omega}[k] = \frac{\Delta\theta[k]}{T_s} = \frac{1}{T_s} \arctan\left(\frac{r[k-1] \otimes r[k]}{r[k-1] \bullet r[k]}\right) \quad (21)$$

The estimation of frequency ω , denoted $\hat{\omega}$, can be computed obtaining the mean value of $\hat{\omega}[k]$ through a discrete LPF

$$\hat{\omega}[k] = a \operatorname{sat}\left[\frac{1}{T_s} \arctan\left(\frac{r[k-1] \otimes r[k]}{r[k-1] \bullet r[k]}\right)\right] + b \hat{\omega}[k-1] \quad (22)$$

where $a = 1 - e^{-\sigma T_s}$ and $b = e^{-\sigma T_s}$, which are obtained through zero-order hold discretisation of the LPF used in (18).

4 Simulation and experimental results

In this section, the simulation and experimental results obtained for the system shown in Fig. 1 are presented. The experimental results were obtained using a VSC prototype with a power rating of 5.4 kVA for a 220 Vrms nominal phase voltage. This VSC was built using discrete IRG4PH50UD IGBTs. The VSC was connected to a strong grid through a three-phase variac, which reduced the actual voltage to 110 Vrms. This variac is modelled in Fig. 1 as the grid inductance $L_g = 90 \mu\text{H}$, and was used to avoid exceeding the maximum voltage of the available non-linear load. The impedance of this inductance is 0.013 pu (base impedance 2.24 Ω), therefore the variac also represents a strong grid. This load was implemented using a three-phase diode bridge and a Sorensen SLH-500-6-1800 Active load. The controller and system parameters, both for simulation and experimental results, are shown in Table 1. The controller was implemented in a fixed point DSP TMS320F2812 with a clock frequency of 150 MHz. The frequency of the pulse-width modulation used in the VSC was 20 kHz. The sample time was $T_s = 100 \mu\text{s}$. The

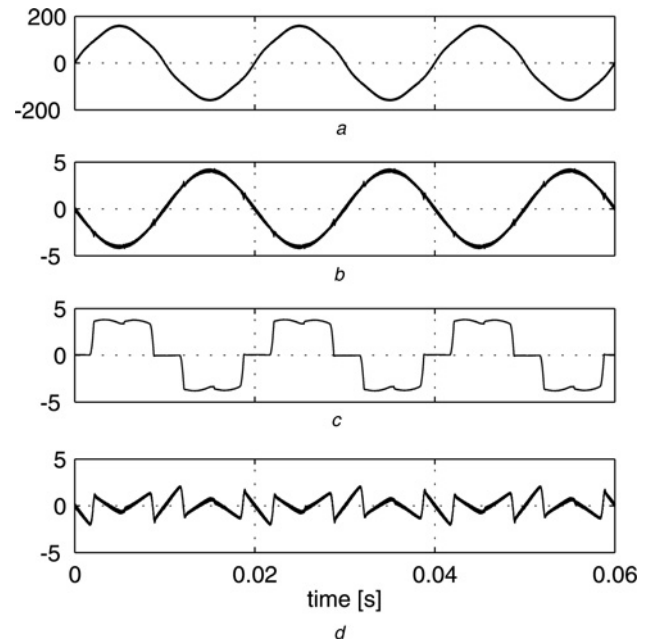


Fig. 5 Simulation results: balanced grid and resistive non-linear load

a Grid voltage
b Grid current
c Load current
d SAPF current

harmonic compensation was performed with $N=14$ and $P=14$, that is, up to the 85th (4250 Hz) harmonic was compensated. Note that for the chosen value of T_s it is not possible to compensate harmonic sequences much higher than this, since it is close to the Nyquist frequency (5 kHz). Also, the bus PI controller gains were chosen empirically in order to obtain a 100 ms transient response to step load changes. For the simulation results the pulse-width modulator (PWM) was included, and a smoothing inductor $L_l = 1 \text{ mH}$ was used (only in simulation). For better simulation accuracy, the controller was implemented using fixed point, as it is actually implemented in the DSP. For the experimental results, all the signals were captured using the high-resolution acquisition mode of the oscilloscope, which filters out the switching ripple. Therefore the actual experimental waveforms have some additional distortion than that shown.

Fig. 5 shows the controller simulation results once the steady state is reached. In Fig. 5a, a grid phase voltage is shown; in Fig. 5b, a grid phase current is shown; in Fig. 5c, a load phase current is shown; and in Fig. 5d, a SAPF

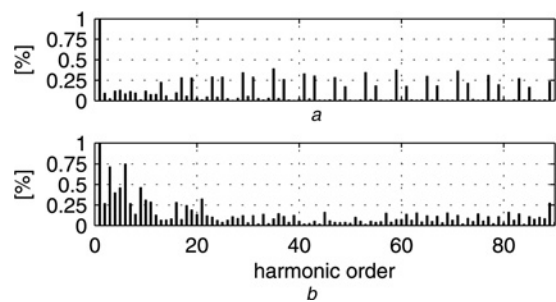


Fig. 6 Current harmonic content

a Simulation results ($\text{THD}_{i_g} = 3.18\%$)
b Experimental results ($\text{THD}_{i_g} = 2.22\%$)

phase current is shown. The harmonic content of the grid phase current is shown in Fig. 6a, which results in a distortion of $\text{THD}_{i_g} = 3.18\%$. In this simulation the grid voltage distortion was $\text{THD}_{v_g} = 3.7\%$ and the load current distortion was $\text{THD}_{i_{nl}} = 28.29\%$. The additional harmonics that appear in the figure are attributed to the PWM and to the quantisation error of implementing the controller in fixed point. As can be seen, proposed controller is capable of achieving the consumption of a sinusoidal grid current in phase with the fundamental component of the grid voltage. The grid current distortion is below that suggested by IEEE Std 519-1992 [1], which validates the controller's harmonic attenuation capability.

Fig. 7 shows the simulation results once the steady state is reached for a load composed of the previous non-linear load in parallel with a three-phase inductive load of 50 mH. Also, to show the performance under normal grid voltage imbalances, the grid voltage was forced to have a 2% imbalance. As can be seen, for an inductive load the controller is still capable of achieving the consumption of a sinusoidal grid current in phase with the fundamental component of the grid voltage. The resulting currents are slightly more distorted than in the previous simulation because the grid voltage imbalance generates current harmonics which are not compensated by the controller. However, the distortion levels are still within the values suggested by IEEE Std 519-1992 [1]. These are, $\text{THD}_{i_{RST}} = 5.66\%/4.2\%/4.87\%$ for phases R, S and T,

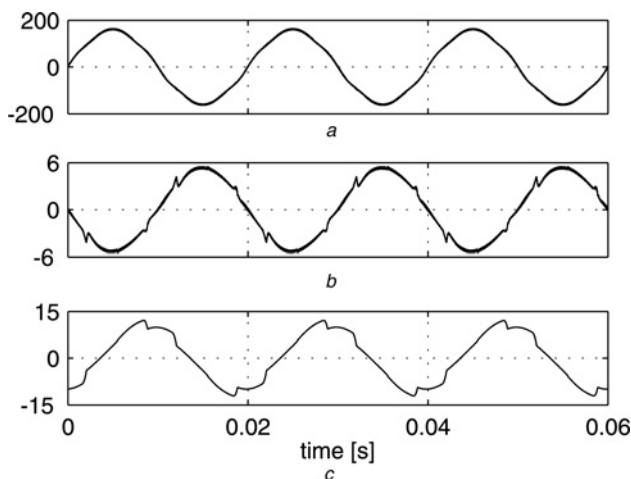


Fig. 7 Simulation results: grid with 2% imbalance, inductive load in parallel with resistive non-linear load

a Grid voltage
b Grid current
c Load current

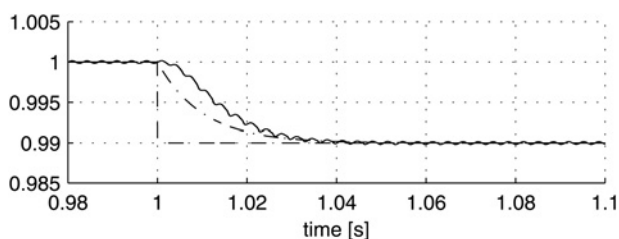


Fig. 8 Simulation results: frequency estimator

Instantaneous grid frequency (dashed line), estimated frequency (solid line), LPF response to a step input (dashed-dot line)
All normalised with respect to ω_0

respectively. In this simulation, the load had an average power consumption of 672 W and 575 VAR, and a current distortion of $\text{THD}_{i_{RST}} = 9.38\%/9.9\%/10.03\%$. The grid voltage distortion was $\text{THD}_{v_g} = 3.63\%/3.69\%/3.68\%$. To verify the behaviour of the frequency estimator, Fig. 8 shows the transient response of (22) when ω has a step variation of -1% . This figure also shows the dynamic response of a LPF with cut-off frequency σ to an

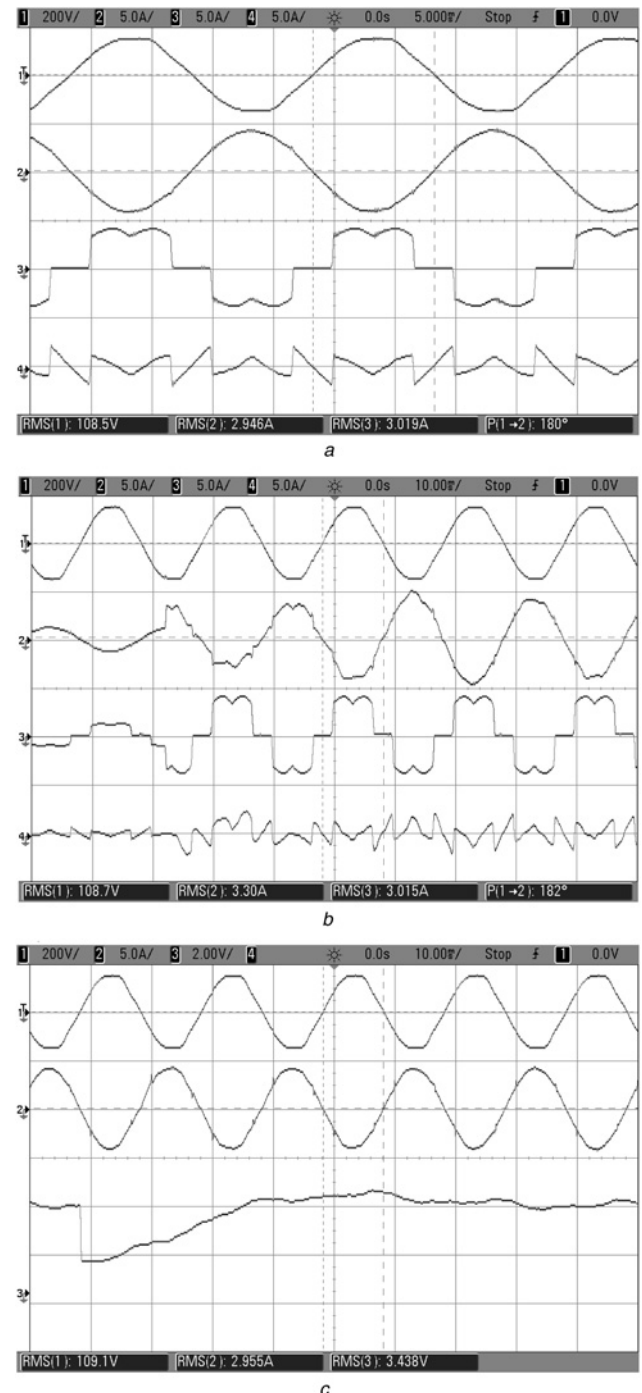


Fig. 9 Experimental results

a Steady-state (timescale: 5 ms/div).

From top to bottom, grid voltage (200 V/div), grid current (5 A/div), load current (5 A/div) and SAPF current (5 A/div)

b Load change (same signals as in (a), timescale: 10 ms/div)

c Estimated frequency variation (timescale: 10 ms/div)

From top to bottom, grid voltage (200 V/div), grid current (5 A/div) and estimated frequency [ω_0 (2/225 div + 443/450)]

input step of the same magnitude. All the signals shown are normalised with respect to ω_0 . These results were obtained once the simulation of Fig. 5 reached steady state. As can be seen, the estimator setting time is $t_{\text{set}} \simeq 40$ ms in concordance with (19) and the value of σ defined in Table 1. It is therefore verified that (19) is a good approximation of the setting time of (18).

Fig. 9 shows the experimental results. In Figs. 9a and b, the signals shown are, from top to bottom, the captures on one phase of: the grid voltage, the grid current, the load current and the SAPF current. For Fig. 9c, the signals are, from top to bottom: the grid voltage, the grid current and the estimated frequency. For these tests the grid voltage THD was $\text{THD}_{V_g} = 3.67\%$, whereas the non-linear load THD was $\text{THD}_{i_{nl}} = 29.4\%$.

In Fig. 9a, the steady-state system response is shown. As can be seen, the resulting grid current has low distortion, which results $\text{THD}_{i_g} = 2.22\%$. The harmonic content of this current is shown in Fig. 6b. In Fig. 9b, the controller transient response to a sudden non-linear load change (from 200 to 70 Ω) is shown. As this figure shows, the controller compensates the load change in approximately 60 ms. Although it might seem like a long transient time, the controller implementation has $2(N+P)+1 = 57$ dynamic states, therefore the dynamic response is fast for this high-order system. Finally, in Fig. 9c, the frequency estimator transient response is shown. To do so, at an arbitrary time instant the estimated frequency is forced to $0.99 \omega_0$. As can be seen, the estimator converges in approximately $t_{\text{set}} \simeq 40$ ms in concordance with (19) and the value of σ defined in Table 1. Also, no significant current perturbations are observed during the frequency transient.

To verify that the bus controller is working properly, Fig. 10 shows the effect of sudden load changes on the bus voltage (from no-load to full-load). As the figure shows, the bus voltage transients converge in about 100 ms, as expected.

The computational burden of the controller without the harmonic compensation ($N+P=0$) is $5.3 \mu\text{s}$, from which $1 \mu\text{s}$ are required for the frequency estimation, and the remaining time is required for computing (3) and the bus controller. Adding ROIGs increases the computational burden by $1.59 \mu\text{s}/\text{ROIG}$. Therefore, the implemented controller, which as $N+P=28$, requires approximately 50

μs , half the available computation time for $T_s = 100 \mu\text{s}$. If the analogue-to-digital converter capture time is added to this ($\sim 13 \mu\text{s}$), the available computation time decreases even further. In case that the DSP is required to implement additional computation tasks (such as communications, protections etc.) the number of ROIGs can be reduced to $N+P=16$ (harmonic 49, 2450 Hz) and still achieve a THD_{i_g} that fulfills the requirements established by the IEEE Std 519-1992. In this case, the computation time will be approximately $30 \mu\text{s}$, freeing a significant amount of computation power.

5 Conclusions

An application to SAPF of a ROIG-based controller for a three-phase system has been presented. This controller does not require a dedicated synchronisation algorithm, and it is grid frequency adaptive. The frequency estimation algorithm is simple, and has a convergence speed comparable to that of more complex strategies. The low-computational burden of this algorithm frees resources for the harmonic compensation task. Since the controller is frequency adaptive it has very good steady-state harmonic rejection capabilities, even when the grid frequency deviates from its nominal value. The application of the ROIG-based controller has been validated through a steady-state analysis, which shows the harmonic rejection capabilities both from the non-linear load and from the grid voltage. Also, simulation and experimental results have been presented. These results show that the transient response of the controller to sudden load changes is satisfactory for the resulting high dynamic order controller.

6 References

- 1 'IEEE recommended practices and requirements for harmonic control in electrical power systems', IEEE Std 519-1992, 1993
- 2 Garcia-Cerrada, A., Pinzon-Ardila, O., Feliu-Batlle, V., Roncero-Sanchez, P., Garcia-Gonzalez, P.: 'Application of a repetitive controller for a three-phase active power filter', *IEEE Trans. Power Electron.*, 2007, **22**, (1), pp. 237–246
- 3 Pigazo, A., Moreno, V., Estebanez, E.: 'A recursive park transformation to improve the performance of synchronous reference frame controllers in shunt active power filters', *IEEE Trans. Power Electron.*, 2009, **24**, (9), pp. 2065–2075
- 4 Kedjar, B., Al-Haddad, K.: 'Dsp-based implementation of an lqr with integral action for a three-phase three-wire shunt active power filter', *IEEE Trans. Ind. Electron.*, 2009, **56**, (8), pp. 2821–2828
- 5 de Araujo Ribeiro, R., de Azevedo, C., de Sousa, R.: 'A robust adaptive control strategy of active power filters for power-factor correction, harmonic compensation, and balancing of nonlinear loads', *IEEE Trans. Power Electron.*, 2012, **27**, (2), pp. 718–730
- 6 Tang, Y., Loh, P.C., Wang, P., Choo, F.H., Gao, F., Blaabjerg, F.: 'Generalized design of high performance shunt active power filter with output lcl filter', *IEEE Trans. Ind. Electron.*, 2012, **59**, (3), pp. 1443–1452
- 7 Rodríguez, P., Luna, A., Muñoz-Aguilar, R., Etxeberria-Otadui, I., Teodorescu, R., Blaabjerg, F.: 'A stationary reference frame grid synchronization system for three-phase grid-connected power converters under adverse grid conditions', *IEEE Trans. Power Electron.*, 2012, **27**, (1), pp. 99–112
- 8 Odavic, M., Biagini, V., Zanchetta, P., Sumner, M., Degano, M.: 'One-sample-period-ahead predictive current control for high-performance active shunt power filters', *IET Power Electron.*, 2011, **4**, (4), pp. 414–423
- 9 Suresh, Y., Panda, A., Suresh, M.: 'Real-time implementation of adaptive fuzzy hysteresis-band current control technique for shunt active power filter', *IET Power Electron.*, 2012, **5**, (7), pp. 1188–1195
- 10 Mikkili, S., Panda, A.: 'Simulation and real-time implementation of shunt active filter id-iq control strategy for mitigation of harmonics with different fuzzy membership functions', *IET Power Electron.*, 2012, **5**, (9), pp. 1856–1872



Fig. 10 Experimental results (timescale: 50 ms/div)

Bus voltage variation on load turn on and turn off
From top to bottom, V_{dc} (100 V/div), I_g^R (5 A/div), I_g^S (5 A/div) and I_g^T (5 A/div)

- 11 Teodorescu, R., Liserre, M., Rodríguez, P.: Grid converters for photovoltaic and wind power systems' (ISBN: 978-0470057513, Wiley-IEEE., 2011)
- 12 Rodríguez, P., Luna, A., Candela, I., Mújal, R., Teodorescu, R., Blaabjerg, F.: 'Multiresonant frequency-locked loop for grid synchronization of power converters under distorted grid conditions', *IEEE Trans. Ind. Electron.*, 2011, **58**, (1), pp. 127–138
- 13 Xiaoqiang, G., Weiyang, W., Zhe, C.: 'Multiple-complex coefficient-filter-based phase-locked loop and synchronization technique for three-phase grid-interfaced converters in distributed utility networks', *IEEE Trans. Ind. Electron.*, 2011, **58**, (4), pp. 1194–1204
- 14 Gomez Jorge, S., Busada, C., Solsona, J.: 'Frequency adaptive discrete filter for grid synchronization under distorted voltages', *IEEE Trans. Power Electron.*, 2012, **27**, (8), pp. 3584–3594
- 15 Busada, C.A., Gomez-Jorge, S., Leon, A.E., Solsona, J.A.: 'Current controller based on reduced order generalized integrators for distributed generation systems', *IEEE Trans. Ind. Electron.*, 2012, **59**, (7), pp. 2898–2909
- 16 Gomez Jorge, S., Busada, C., Solsona, J.: 'Frequency-adaptive current controller for three-phase grid-connected converters', *IEEE Trans. Ind. Electron.*, 2013, **60**, (10), pp. 4169–4177
- 17 Martin, K.: 'Complex signal processing is not complex', *IEEE Trans. Circuits Syst. I, Regul. Pap.*, 2004, **51**, (9), pp. 1823–1836
- 18 'IEEE recommended practice for monitoring electric power quality', IEEE Std 1159-2009 (Rev. of IEEE Std 1159-1995), 2009, pp. 1–81
- 19 Vaccaro, R.J.: 'Digital control: a state-space approach' (McGraw-Hill, Inc, 1995)
- 20 Bryson, A.E., Ho, Y.-C.: 'Applied optimal control: optimization, estimation, and control' (ISBN: 978-0470114810. John Wiley & Sons., 1975)